

High-amplitude, ultrashort strain solitons in solids

Otto L. Muskens and Jaap I. Dijkhuis

*Atom Optics and Ultrafast Dynamics, Debye Institute, Department of Physics and Astronomy,
University of Utrecht, P.O. Box 80000, 3502 TA, Utrecht, The Netherlands*

1 Introduction

1.1 Historical perspective

1.2 Nano-ultrasonics

1.3 Shock waves and strain solitons

2 Theory of strain solitons

2.1 Nonlinear elasticity

2.2 One-dimensional propagation

2.3 Soliton trains

2.4 Shock wave development

2.5 Discrete and higher-dimensional models

3 Simulations

3.1 Soliton trains in sapphire

3.2 Diffraction and soliton formation

3.3 Stability of individual solitons

4 Brillouin scattering experiments

4.1 Introduction

4.2 Setup

4.3 Transition from shock waves to soliton trains

4.4 Diffraction and the formation of solitons

5 Conclusions and Prospects

1 Introduction

In this chapter, we review recent experiments on the development of ultrashort acoustic solitons from intense picosecond strain wavepackets. High-amplitude bipolar wavepackets are injected by the impact of mJ femtosecond pulses from an amplified Ti-sapphire laser on a thin chromium film evaporated on the surface of the sapphire crystal. Under these conditions, the combined action of nonlinearity of the lattice and phonon dispersion leads to the formation of trains of stable acoustic solitons after propagation distances of hundreds of micrometers. This we demonstrated by numerical simulations of the Korteweg-de-Vries equation and extensive Brillouin scattering experiments [1,2]. The ultrafast character of these soliton pulses was proved by experimentally demonstrating impulsive excitation of the 1-THz crystal-field transition in optically excited ruby [3].

From this we may conclude for sapphire that we generate millimeter-wide, nanometer-thick, supersonic disks with pressures as high as tens of kilobars. We will briefly speculate on the possible use of these extraordinary nano-ultrasonic pulses for constructing a phonon laser, for generating terahertz surface plasmons in piezoelectric epitaxial layers, and perhaps for exciting nano-ultrasonic surface waves.

1.1 Historical perspective

The spectrum of acoustic waves that can be excited in condensed matter spans over 15 orders of magnitude. Figure 1 shows this acoustic frequency spectrum together with some important applications in technology and everyday life. As the acoustic frequency scales up, the

corresponding wavelength shifts down to regimes that are of interest for modern solid-state technological applications.

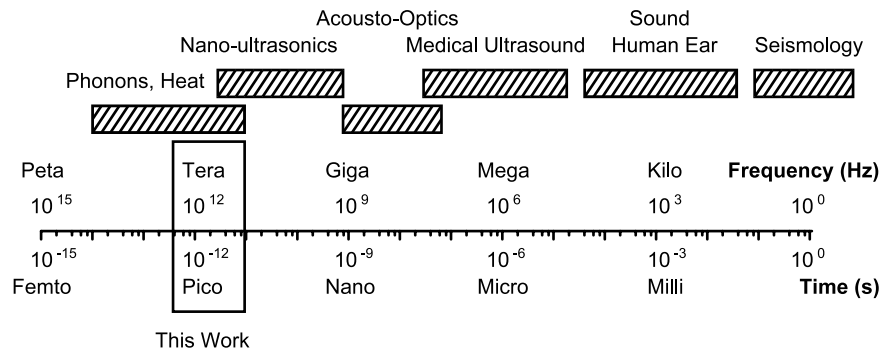


Figure 1 Acoustic-wave spectrum between 10^0 and 10^{15} Hz, with corresponding time scale in seconds. Shaded blocks denote the typical application windows of acoustic waves in technology and everyday life. Rectangle denotes the frequency range of the picosecond acoustic pulses that form the topic of this chapter.

The generation of coherent, longitudinal acoustic waves, and more specifically the formation of short, stable acoustic pulses, has been an active topic for decades. Extension towards high frequencies of operation, although challenging, has for a long time merely been a technological issue. The development and optimization of thin-film piezoelectric resonators has enabled ultrasonic applications up to gigahertz frequencies [4]. However, conventional electro-acoustic methods reach their practical limit at this point, and several other schemes have been attempted to approach the regime of terahertz coherent phonons. Grill and Weis [5] reported surface generation of coherent phonons by direct conversion of infrared laser radiation in a piezoelectric crystal. The efficiency of this process however turned out to be greatly influenced by the quality of the crystal surface, preventing its use for practical applications. Another line of research

consists of the generation of a macroscopic acoustic field using electronic two-level systems, such as found in paramagnetic impurity ions. The interaction of gigahertz ultrasonic waves with these centers was developed experimentally by Shiren [6], and described theoretically by Jacobsen and Stevens [7]. Tucker [8] showed that, after population inversion of the electronic system, it may release its energy in the form of stimulated emission of phonons. An important step forward was made by the application of terahertz two-level systems found in transition metal ions, which have excited-state multiplets that can be simply inverted using optical radiation and that decay via a single-phonon transition. Many studies have been conducted on stimulated emission in these systems [9-13], but most of them could be explained by incoherent rate-equations, leaving controversy over the degree of coherence reached in the acoustic field.

1.2 Nano-ultrasonics

A completely new field of optoacoustics has emerged by the development of picosecond pulsed lasers [14]. Ultrafast optical excitation of metal films allows for a relatively direct generation of pressure pulses, which can subsequently be used to probe nanometer-sized structures in an otherwise opaque substrate. This method of picosecond ultrasonics has developed since the mid-eighties into a well-established technique for studying multilayers both in fundamental research and in the semiconductor industry. Only recently new applications have emerged, which explore the use of nano-ultrasonic pulses in other directions. We categorize some of these novel research perspectives into the following main categories [c.f. Fig. 2(a)]:

1. Analysis of thin-films, multilayers, and nanostructured media [14-16].

2. Excitation of semiconductor embedded structures, quantum wells, and piezoelectric materials [17-19].
3. Imaging of single nano-objects and of local elastic properties, using a combination of nano-ultrasonics and microscopy [20,21].
4. Coherent phonons in two-level media and the construction of a phonon LASER [3].
5. Long-distance propagation, dispersion, diffraction, and soliton formation [1,2,22-26].

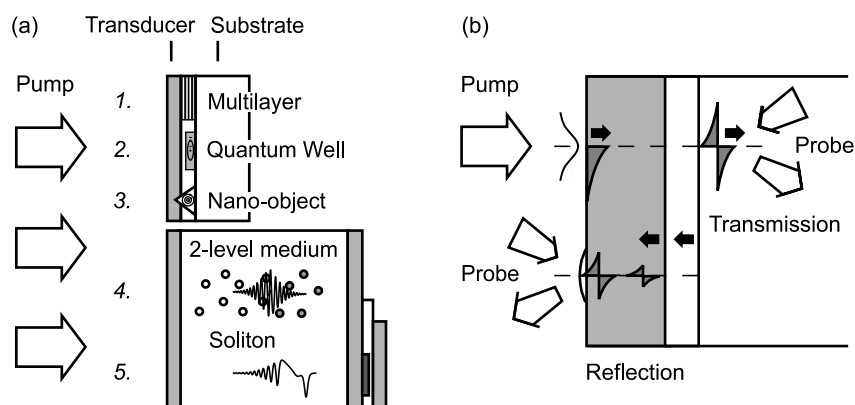


Figure 2 (a) Directions of research using nano-ultrasonic pulses, numbers refer to topics in text. (b) Principle of picosecond ultrasonics, using ultrafast thermoelastic excitation and subsequent detection of either the reflected echoes or of the transmitted wavepacket.

The principle of operation of the picosecond acoustic method is shown in Fig. 2(b). Ultrafast optical pulses are used to excite the electron gas via intra- or interband absorption in the first few nanometers of the absorbing layer. The excess energy in the promoted electrons is redistributed over the other carriers via electron-electron interactions within tens of femtoseconds, and subsequently transferred to the lattice through electron-phonon coupling within less than a picosecond. Depending on the exact mechanism involved, either thermo-elasticity for metals or athermal bond-switching processes for semiconductors, this energy is converted into a coherent

compression or expansion of the lattice. When the area of excitation is much larger than the optical skin depth, a plane-wave is launched in both directions perpendicular to the surface. The part traveling to the stress-free surface is reflected with a phase change, resulting in a release wave following the compressive wave and vice versa. At interfaces or embedded objects inside the material, a part of the bipolar wavepacket is reflected back towards the surface. The arrival of these acoustic echoes at the surface can be detected using time-resolved reflectometry or interferometry, yielding information on the internal structure.

1.2 Strain Solitons and Shock Waves

Whereas picosecond ultrasonics has focused on propagation of strain pulses over submicrometer distances for many years, long-distance transport has been explored only recently. In transport experiments, information can be obtained on fundamental material properties that exert their influence only after long distances of propagation. Some established methods, well equipped at detecting strain over large distances, have recently been adapted to study terahertz coherent phonon wavepackets. Examples of these are the superconducting phonon bolometer (this volume, chapter by Kent), the Brillouin scattering method described in this chapter [1,2], and the ruby phonon spectrometer of Ref. [3]. Additionally, picosecond time-resolved methods have recently demonstrated their value in long-distance transport experiments as well. Duquesne and Perrin [22] determined ultrasonic attenuation in a quasicrystal using picosecond interferometry. Daly et al. [23] studied the influence of diffraction on small-area picosecond acoustic pulses and recovered two-dimensional information using a sophisticated imaging algorithm. In a series of experiments, Hao and Maris [24, 25] demonstrated the influence of phonon dispersion on the

propagation of picosecond strain wavepackets. They showed that after several hundreds of micrometers, the wavepackets are severely distorted by the dispersion of the longitudinal acoustic phonons. Thus, for the first time it seemed that the stability of short acoustic pulses is limited by fundamental physical restraints rather than by technological issues.

However, as we will show later on, at larger strain amplitudes, nonlinear contributions emerge that can partially cancel the effect of the dispersive destruction of the pulse shape. In their experiments, Hao and Maris demonstrated the development of an archetypical *solitary* wave [26]. Solitons have been found in many other physical systems combining dispersion and nonlinearity, but were never before demonstrated for picosecond strain pulses in crystalline solids. The solitons, which are of the compressive kind, travel with a supersonic velocity through the crystal. This property allowed their separation from the remaining wavepacket in time-resolved experiments.

These first investigations of the phonon solitons used nanojoule optical pulses to excite and to probe the picosecond strain packets. The optical power of such a system is however insufficient to enter far into the soliton regime. Investigations were limited to intermediate strain values of the order of 10^{-4} and to narrow strain pencils, due to the necessity of tight focusing of the pump laser. Furthermore, to improve the effect of acoustic nonlinearity, a thin-film transducer had to be constructed that delivered very high frequency strain pulses (of up to 300 GHz), requiring a very high quality of the contact interface of the substrate and the transducer.

In order to extend the regime of strain amplitudes significantly, we developed new experiments on acoustic solitons, using high-power optical pulses from an amplified ultrafast laser system as the excitation source [1-3]. In this way we can routinely generate high aspect-ratio (up to $1:10^5$), plane-wave picosecond strain packets with very high amplitudes (0.4% strain in the metal film), which may be very suitable for technological applications. Further, we use a relatively thick, 100-nm chromium transducer, which produces strain pulses with initial acoustic frequency components below 100 GHz. As we will show below, this does not prevent the formation of terahertz acoustic solitons, as the large strains ensure a fast nonlinear evolution of the pulse into a shock wave structure.

Under high-power excitation, the formation of a shock front occurs in a distance of less than a hundred micrometers, the distance over which the strain pulse steepens up by the velocity increase of the high-amplitude peak with respect to the low-amplitude front. As the slope of the shock front increases, higher frequency components are generated in the acoustic wave spectrum. At elevated temperatures, thermal scattering will result in strong dissipation of these high-frequency components, flattening out the shock. At low temperatures however, thermal scattering is small and the high-frequency components of the pulse survive. As a result, phonon dispersion comes into play as terahertz-frequencies are being generated at the steep front. The combined action of nonlinearity and dispersion leads to a breakup of the shock wave into a train of stable, ultrashort solitons. As the ratio between nonlinear and dispersive behavior grows with increasing strain amplitudes, the solitons shorten and the train grows up to many solitons, depending on the crystal, transducer materials, and excitation powers used.

The development of high-amplitude, ultrashort strain solitons opens up a variety of technological perspectives. A lot has been learned on the behavior of solids under high hydrostatic pressure under steady-state conditions [29]. High-pressure shock wave experiments with nanosecond time resolution have further revealed the equation of state (EOS) of many materials [30]. The novel perspective to generate, nondestructively, high-amplitude strain pulse of *ultrashort* time duration allows for a novel domain of dynamical high-pressure experiments. The strains reached in our experimental work (0.1-1%) are close to the plasticity threshold for many solids, and irreversible behavior may be expected under these extreme conditions. High-pressure pulses of ultrashort time duration might therefore be applied to modify material properties with nanometer precision. The influence of high-amplitude, ultrashort strain pulses on important material properties like the nature of the vibrational modes in amorphous solids or the local structure around impurity or dopant ions in a semiconductor has yet to be investigated. Semiconductor physics would certainly benefit from such a source of high-intensity acoustic strain. The acoustic wavelength of several nanometers in principle allows for a very high spatial resolution for imaging or manipulation of materials. The sensitivity for the local elasticity of the material provides a novel contrast mechanism for imaging nanostructures [23].

2 Theory of strain solitons

In this section we start with a brief overview over the classical theory of nonlinear elasticity for finite deformations. In contrast to the theory of infinitesimal elasticity, that was already well-developed in the beginning of the twentieth century [29], extension to intermediate strains was taken up seriously in the early fifties [30]. Closely related to the theory of fluid mechanics, solid-

state models have been developed in the continuum limit and in the language of the bulk elasticity parameters. This approach results in a dispersionless theory, and lattice dispersion can only be included a posteriori, in an artificial way. Therefore we also mention the existence of paths leading to the nonlinear dispersive wave equation that start from a microscopic picture. Then, after transformation to traveling coordinates, we readily arrive at the well-known Korteweg-de Vries (KdV) equation, that has stable solutions in the form of *solitary waves* [31,32]. It is shown that an initial compressive strain pulse breaks up into a train of such solitons. We consider the effect of temperature on the wavepacket development and briefly present the theory for shock waves using the Burgers equation. The section is concluded by an extension of the nonlinear dispersive wave equation to include diffraction.

2.1 Nonlinear elasticity

In this overview of nonlinear elasticity theory we follow the derivation and nomenclature as presented in the review of Wallace [33]. First, a set of curvilinear coordinates is introduced and the local deformation and strain variables are derived in this basis. Throughout the text we will be using the Einstein summation convention.

Let us consider an undeformed solid in which a point is denoted by the vector $\vec{r} = r_j \vec{a}_j$ with respect to the basis \vec{a}_j of the crystal. In an arbitrary deformed state, the position of the vector changes to $\vec{r}' = \vec{r} + \vec{u}(\vec{r}, t)$, with $\vec{u}(\vec{r}, t)$ the local displacement vector corresponding to the deformation. The above definitions also permit transformations that do not distort the internal material structure, like uniform translation and rotation. An adequate definition of local

deformation that filters out these simple transformations is the length change, or deformation Δ , of a local vector $\vec{r} = \vec{r}_2 - \vec{r}_1$, that can be written in the form

$$\Delta = |\Delta\vec{r}'|^2 - |\Delta\vec{r}|^2 = 2\eta_{ij}\Delta r_i\Delta r_j. \quad (1)$$

The right hand side of Eq. (1) has been obtained by expanding the squared terms using $\vec{u}(\vec{r}_2, t) - \vec{u}(\vec{r}_1, t) = \nabla\vec{u}(\vec{r}, t)\Delta\vec{r}$. The matrix connecting the initial configuration \vec{r} to the deformation Δ is called the strain matrix η , and follows from Eq. (1) as

$$\eta_{ij} = \frac{1}{2}(u_{ij} + u_{ji} + u_{ik}u_{kj}), \quad (2)$$

where $u_{ij} = \partial u_i / \partial r_j$ describes the displacement gradient matrix elements. The above description holds as long as variations in the displacement gradients take place on a length scale much larger than the differential elements $\Delta\vec{r}$. In practice this means that the strain must be smooth on the scale of the interatomic distances in the solid.

The most important consequence of Eq. (1) is that related quantities like the free energy at finite strain can be expressed in terms of the undeformed coordinates \vec{r} and the strain matrix η . For example, one can expand the internal energy Φ per unit of mass in terms of strain according to

$$\rho\Phi_S(\vec{r}, h) = \rho\Phi_0 + C_{ij}\eta_{ij} + \frac{1}{2}C_{ijkl}\eta_{ij}\eta_{kl} + \frac{1}{6}C_{ijklmn}\eta_{ij}\eta_{kl}\eta_{mn} + \dots \quad (3)$$

Here ρ is the mass density and the subscript S denotes that the deformation takes place at constant entropy, i.e. under adiabatic conditions. The constants C are the elasticity constants of first, second and third order, respectively, defined by the first- and higher-order partial derivatives of the internal energy to the strain elements $C_{ij} = \partial\Phi_S / \partial\eta_{ij}$, $C_{ijkl} = \partial^2\Phi_S / \partial\eta_{ij}\partial\eta_{kl}$, etc.

For a simple, one dimensional spring, one can calculate the force resulting from a compression by taking the derivative of the internal energy to the displacement (Hooke's law). On a similar vein, one can calculate the induced stresses for finite deformation using simple thermodynamic considerations [33]. For a stress-free initial state, the stress-strain relation reads

$$T_{ij} = \rho \frac{\partial \Phi_S(\bar{r}, \eta)}{\partial \eta_{ij}}. \quad (4)$$

The equation of motion for finite strains can now be formulated in terms of this stress tensor and the mass density ρ . The Euler-Lagrange equations of motion for the generalized coordinates $\bar{r}'(\bar{r}, t)$ in the independent variables \bar{r} and t read

$$\frac{\partial}{\partial t} \frac{\partial L}{\partial \dot{r}'_i} + \frac{\partial}{\partial r'_k} \frac{\partial L}{\partial \alpha_{ik}} = 0, \quad (5)$$

with the abbreviation $\alpha_{ik} = \partial r'_i / \partial r'_k$. The Lagrangian density can be written as the difference of kinetic and potential energy, which for adiabatic deformation gives

$$L = \frac{1}{2} \rho \dot{r}'_i \dot{r}'_i - \rho \Phi_S(\bar{r}, t). \quad (6)$$

Combining Eqs. (5) and (6), one arrives at the equation of motion

$$\rho \ddot{r}'_i = \rho \frac{\partial}{\partial r'_k} \left(\frac{\partial \Phi_S}{\partial \eta_{lm}} \right) \frac{\partial \eta_{lm}}{\partial \alpha_{ik}}. \quad (7)$$

Using the relation $\partial \eta_{lm} / \partial \alpha_{ik} = \delta_{il} \delta_{km}$ for a stress-free initial state one can simplify the equation of motion, Eq. (7), to a generalized form of Newton's law

$$\rho \ddot{u}_i = \frac{\partial}{\partial r'_k} T_{ik}. \quad (8)$$

Here we have replaced the higher order derivative of \vec{r}' by that of the displacement vector \vec{u} , which is allowed by its definition in Eq. (1). With the combination of Eq. (8), the stress-strain relation Eq. (4), and the free energy expansion Eq. (3), we now have all the ingredients to compose a nonlinear acoustic wave equation. Keeping only terms up to second order in derivatives of u , this equation of motion can be rearranged into the form

$$r\ddot{u}_i = \frac{\partial u_{jk}}{\partial r_l} (C_{ijkl} + u_{pq} A_{ijklpq}). \quad (9)$$

It should be noted that the term A_{ijklmn} contains a combination of third-order *and* second order elastic constants:

$$A_{ijklpq} = C_{jlpq} \delta_{ik} + C_{ijql} \delta_{kp} + C_{jkql} \delta_{ip} + C_{ijklpq}. \quad (10)$$

The second-order coefficients in this expression are a consequence of the presence of the quadratic term in the definition of strain, Eq. (2). Therefore, these contributions to the nonlinear term in the propagation equation, Eq. (9), are sometimes referred to as the *geometrical* nonlinearity, whereas the third order constants are called the *physical* nonlinearity. One may convert the elastic constants in Eq. (9) to tabulated values in Voigt notation by the reduction of pairs of indices [34].

2.2 One-dimensional propagation

In the case of an acoustic plane-wave along an axis of high symmetry z , the equation of motion, Eq. (9), reduces to the simple form

$$\rho u_{tt} = \gamma u_{zz} + \alpha u_z u_{zz}, \quad (11)$$

where the subscripts denote differentiation. The last term on the right side is the quadratic nonlinearity, owing to the geometric nonlinearity and the cubic terms in the inter-atomic potential. The nonlinearity coefficient α depends only on the propagation direction in the crystal. For the [0001]-direction in a trigonal crystal like sapphire, for example, the two constants of Eq. (11) can be found from Eq. (10) as

$$\gamma = C_{33}, \alpha = (3C_{33} + C_{333}), \quad (12)$$

where the coefficients C_{33} and C_{333} are the second- and third-order elastic constants in the [0001]-direction. For most solids, the contribution of the third order modulus is larger than the geometric term and has a negative sign, yielding a negative nonlinearity α .

Up to this point we have not taken into account any dispersion in the equation of motion. In the case of longitudinal acoustic lattice vibrations (LA phonons) in a trigonal crystalline solid in the direction of the c axis ([0001]), the dispersion due to discreteness of the lattice can be written up to third order as [35]

$$\begin{aligned} \omega &= c_0 k - \beta k^3. \\ \beta &= \frac{c_0 a^2}{24} = \frac{c_0^3}{6\omega_{\max}^2}, \end{aligned} \quad (13)$$

where $\omega_{\max} = (4C_{33}/M)^{1/2}$ is the LA angular frequency at the edge of the Brillouin zone, and $c_0 = (C_{33}a^2/M)^{1/2}$ denotes the sound velocity. This dispersive correction can be put into Eq. (11), leading to a fourth order spatial derivative. At this point it is convenient to switch from the displacement coordinate u to a uniaxial component of the acoustic strain, further denoted as s . This is done by differentiation of Eq. (11) with respect to the z -coordinate. Given the initial

wave packet at $t = 0$ of amplitude s_0 and shape $\phi(z)$, the resulting boundary value problem including dispersion, reads

$$\begin{aligned} s_{tt} - c_0^2 s_{zz} - \frac{\alpha}{\rho} \frac{\partial}{\partial z} (s s_z) - 2c_0 \beta s_{zzz} &= 0 \\ s(z, t = 0) &= s_0 \phi(z). \end{aligned} \quad (14)$$

Finally it is convenient to transform to a moving frame coordinate system, defined by the parameters $t' = \varepsilon t$, $y = z - c_0 t$, where the small constant ε is used to express the slowness of the time coordinate. After substitution of these variables and maintaining terms up to order ε we arrive at terms consisting of only one derivative with respect to the traveling coordinate y .

Integrating the resulting expression once, we finally obtain the equation

$$\begin{aligned} s_{t'} + \frac{\alpha}{2\rho c_0} s s_y + \beta s_{yyy} &= 0 \\ s(y, t' = 0) &= s_0 \phi(y). \end{aligned} \quad (15)$$

This is the well-known Korteweg-de Vries (KdV) equation, describing for example the formation of stable wave packets (solitons) in a narrow water channel [31]. In the experimental configuration in the sapphire crystal, $\alpha < 0$ and $\beta > 0$, resulting in soliton development for $s < 0$, i.e. for compressive strain pulses.

2.3 Soliton trains

We are interested in the development of an arbitrary initial waveform $s(y, t) = s_0 \phi(y/l_0)$, where s_0 and l_0 are the typical (negative) strain amplitude and the spatial width of the compressive part

of the initial strain packet. After transformation to the coordinates $\eta = s/s_0$, $\xi = y/l_0$, and $\tau = t'\beta/l_0^3$, the initial value problem of Eq. (15) takes on the form [36]

$$\begin{aligned} \eta_\tau + 6\sigma^2\eta\eta_\xi + \eta_{\xi\xi\xi} &= 0 \\ \eta(\xi,0) &= \phi(\xi), \end{aligned} \quad (16)$$

where σ is a dimensionless parameter defined by

$$\sigma = l_0 \left(\frac{\alpha s_0}{12\rho c_0\beta} \right)^{1/2}. \quad (17)$$

Equation (17) yields identical solutions for initial wavepackets with the same value of σ and $\phi(\xi)$ and therefore σ is called the similarity parameter. The magnitude of σ determines the relation between nonlinearity and dispersion in the wavepacket development. According to Eq. (17), σ is proportional to the area under the square root of the compressive strain waveform. In order to compare the similarity parameters for different initial value conditions, it is thus important to choose l_0 and s_0 so that the residual area of $[\phi(\xi)]^{1/2}$ is normalized to some predefined value, which in Ref. [37] equals π , the area under the square root of the soliton-waveform of Eq. (19).

For the KdV-initial value problem Eq. (16) there exists an associated eigenvalue problem for the Schrödinger equation [38]

$$\Psi_{\xi\xi} + \left(\lambda + \frac{\sigma^2}{6} \eta(\xi, \tau) \right) \Psi = 0. \quad (18)$$

The solutions of this eigenvalue equation can consist of free or bound states, depending on the sign of the initial potential $\phi(\xi)$. The reflection and transmission coefficients can be derived

using the time dependence of the eigenfunctions Ψ , as dictated by the KdV equation for the potential $\eta(\xi, \tau)$. A concise overview of the inverse scattering method for the KdV-initial value problem can be found in Refs. [36,37]. We limit our discussion here to the most relevant result for this chapter, namely the stationary states, when $t \rightarrow \infty$, for the potential $\eta(\xi, \tau)$, for a discrete spectrum of eigenmodes $\lambda_n < 0$. It turns out that all bound states of the initial potential $\phi(\xi)$ correspond to soliton-pulses determined by the eigenvalue λ_n , according to

$$\eta(\xi, \tau) = \frac{-2\lambda_n}{\sigma^2} \operatorname{sech}^2\left(|\lambda_n|^{1/2}(\xi + 4\lambda_n \tau)\right) \quad (19)$$

It can be observed from Eq. (19) that the amplitude of the n -th soliton is $\eta_n = -2\lambda_n / \sigma^2$, or

$a_n = -2\lambda_n s_0 / \sigma^2$ in normal strain units. The velocity of these solitons is $2\eta_n \sigma^2$ in normalized

coordinates, or $c_n = \alpha a_n / 6\rho c_0$ in real coordinates. Finally, the width is given by $[2/\eta_n \sigma^2]^{1/2}$, or

$l_n = l_0 [2s_0 / a_n \sigma^2]^{1/2}$ in normal units.

The exact number of solitons developing from an initial perturbation may be found from the depth of the potential well $\phi(\xi)$ and the spacing of the eigenvalues of the energy. An analytical solution of the eigenvalue equation, Eq. (18) may be obtained in several special cases of the initial waveform $\phi(\xi)$. In particular, the spectrum of eigenvalues for a potential of the form

$\phi(\xi) = \sec h^2 \xi$ can be found in quantummechanical textbooks [39] as

$$\lambda_n = -\frac{1}{4} \left(1 - 2n + \sqrt{1 + 4\sigma^2}\right)^2. \quad (20)$$

However, in our experiments we will be dealing with strain pulses that have not the above form, but a profile given to good approximation by the derivative of a Gaussian. It turns out that the

compressive part of this waveform resembles quite well the hyperbolic secant function, so that we can use Eq. (20) in our estimates for the experimental soliton trains. The corresponding values of σ are to be calculated using Eq. (17) after the appropriate normalization of the compressive waveform [2].

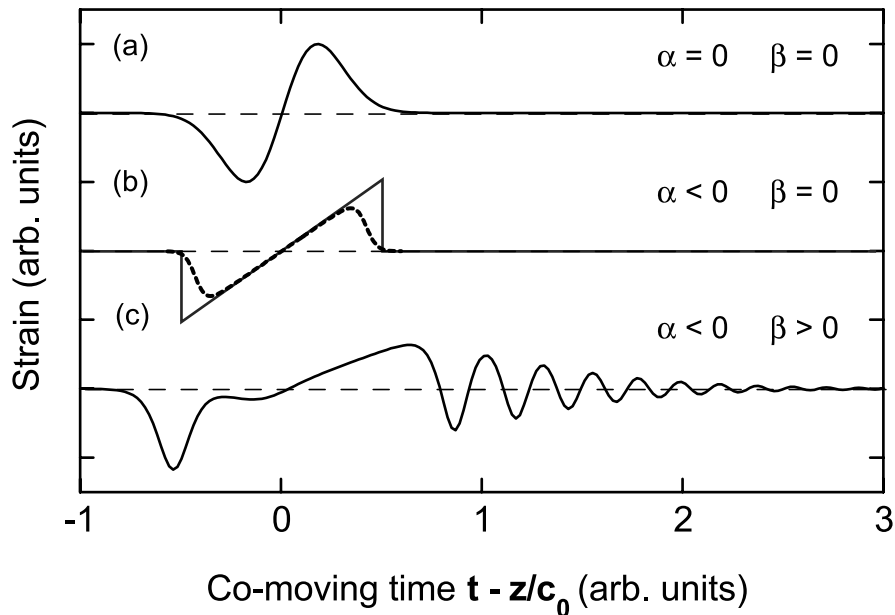


Figure 3 Development of an initial wavepacket for different combinations of nonlinearity α and dispersion β , showing linear propagation (a), typical shock wave formation without (b, line) and with damping (b, thick dash) and soliton development (c), for a similarity parameter $\sigma \approx 1$.

Figure 3 shows the development of a typical initial waveform, in the situations of nonlinear propagation both in absence [Fig. 3(b)] and presence [Fig. 3(c)] of the third-order dispersion.

The dispersionless case results in the formation of shock fronts, the compressive phase of the bipolar wavepacket travelling slightly faster and the rarefaction phase slightly slower than the

linear velocity of sound. This situation will be discussed in Sec. 2.4. The trace including the dispersion shows the development of a soliton pulse in the leading part and a oscillating tail in the trailing part of the bipolar initial wavepacket. The parameters α, β were chosen so that the similarity parameter for the compressional part equals $\sigma \approx 1$, leading to only one negative eigenvalue λ . The radiative tail is associated with the continuum of positive energy states of the scattering problem, Eq. (19). Although analytical expressions for this tail exist in the case of linear dispersive waves [36,37], no simple form is known for the combination of nonlinearity and dispersion in the wavepacket propagation.

Note that, for comparison with experiments, we use in all numerical simulations a boundary value problem instead of an initial value problem, that is equivalent to Eq. (15) after a trivial transformation $t \rightarrow z/c_0, z \rightarrow c_0 t$. The theoretical description was however presented in as an initial value problem for compatibility with the existing literature [36-38].

2.4 Shock wave development

In practice, except at the lowest temperatures, acoustic waves are attenuated by scattering at thermal phonons during propagation through a crystal. Classically, this scattering can be accounted for by including a viscous term in the wave equation

$$\begin{aligned}
 s_t + \frac{\alpha}{2\rho c_0} s s_y - \epsilon s_{yy} + \beta s_{yyy} &= 0 \\
 s(y, t = 0) &= s_0 \phi(y/l_0).
 \end{aligned}
 \tag{21}$$

Here ε denotes the viscosity constant of the medium, which can be obtained experimentally from the thermal scattering length of ultrasonic waves [34]. The combination of nonlinearity, dispersion, and viscosity in the wave equation is called the Korteweg-de Vries-Burgers (KdV-Burgers) equation. Unlike the KdV-initial value problem, this is not an integrable equation and a solution can only be obtained numerically. For special situations, however, we may neglect either one of the three constituent terms and recover the KdV-, Burgers- or a linear wave equation. At this point we will consider the problem of a small dispersive term relative to the viscous term. Neglecting the dispersion, one recovers the Burgers equation that can be solved in an analytical way. Starting from the Burgers equation in the form $s_t + \frac{1}{2}(s^2)_y = \nu s_{yy}$ one can apply the Cole-Hopf transformation $s = -2\nu u_y / u$ to arrive at

$$u_t = \nu u_{yy}. \quad (22)$$

This is the well-known heat equation, which has solutions that spread out diffusively with time [36]. The development of the initial wavepacket depends on the relative magnitude of the nonlinearity and dispersion, as contained in the parameter $\nu = c_0 \varepsilon / \alpha$. The most relevant case for this work is the condition that nonlinearity dominates the wavepacket development. In the extreme case, when viscosity is neglected, the initial shape develops until an infinitely sharp wavefront is formed. For an initially symmetric bipolar waveform it can be shown that, in the limit $y \rightarrow \infty$, it develops into a shape of the form [36]

$$s(t, y) = \begin{cases} y/t & -\sqrt{2A_0 t} < y < \sqrt{2A_0 t} \\ 0 & |y| > \sqrt{2A_0 t} \end{cases}, \quad (23)$$

where A_0 denotes the area under one phase of the initial waveform. The solution for a bipolar wavepacket after a long time in the case of nonzero viscosity can be found using the solution of Eq. (22)

$$s(y,t) = \frac{y}{t} \frac{\sqrt{a/t} \exp(-y^2/4vt)}{1 + \sqrt{a/t} \exp(-y^2/4vt)}. \quad (24)$$

The typical form of a so-called N-wave is shown as the dashed line in Fig. 3(b). This expression can be scaled to the initial waveform via the area under one of its phases, $A_0 = 2\nu R_0$, where we have introduced an initial Reynolds number $R_0 = \log(1 + \sqrt{a/t_0})$. The characteristic property of Eq. (24) is the scaling of the main profile (i.e. the N-structure) over $y = (2A_0 t)^{-1/2}$, combined with a smearing out of the shock front over a distance $\Delta y = R_0^{-1} \log t/t_0$. Further, the integral under each phase of the bipolar wavepacket decays by dissipation through the viscous term as $A(t)/A_0 = \log(1 + \sqrt{a/t} - \exp R_0)$.

2.5 Discrete and multidimensional models

As an extension of the above derivation, we wish to spend some words to a) the approach starting from a discrete model and b) multidimensional corrections to the Korteweg-de Vries equation. The classical theory of finite elasticity resulted in a fully three-dimensional, nonlinear wave equation for arbitrary crystallographic symmetry. After reduction to one dimension, phonon dispersion was added by means of a correction *a-posteriori*. For the problem of ultrashort strain packets in a crystalline lattice, it may well be worth the effort to consider a derivation that maintains the discrete character of the atomic lattice. The theory of nonlinear

lattices has been developed since the early work of Fermi, Pasta and Ulam [40], but has soon focused on analytical model systems in one dimension (see e.g. Ref [41]). In these models, dispersion is an inherent feature of the discrete system, and solitary waves have been identified as the normal modes of the nonlinear lattice. It has been demonstrated that the one-dimensional integrable lattice with exponential interactions, known as the Toda chain [41], reduces to the KdV equation in the long-wavelength limit.

Potapov et al. [42] showed that a two-dimensional microscopic lattice model can be used to derive the nonlinear dispersive wave equation for the atomic displacements. They started from a two-dimensional construction of point masses and considered only nearest-neighbor interactions in the first two configurational shells. Meijer [43] extended this approach to a cubic lattice in three dimensions. In these calculations, the local deformations are again defined by the square of the interatomic distances, similar to Eq. (1), but now on a discrete lattice. Subsequently, the transition from a discrete to a continuous description is made by maintaining second-order term in the expansion for the local displacement gradient $\vec{u}(\vec{r}_2, t) - \vec{u}(\vec{r}_1, t)$. This approach results in a wave equation for the displacement similar to Eq. (14) but with microscopic force constants, demonstrating that the dispersive correction indeed has the form of the a posteriori term introduced in Eq. (13). However, as the elastic constants usually are determined experimentally from the strain derivative of the free energy, the resulting expressions have to be compared with continuum elasticity if one wants to describe an experimental situation.

We now arrive at the addition of diffraction phenomena in the nonlinear dispersive wave equation. In order to investigate the effect of weak higher-dimensional propagation effects, one has to maintain a higher-order term in the transverse gradients of the displacement vector. This

can be done starting from the full three dimensional equation, Eq. (9), by the assumption that the transverse derivatives will have an influence of order $\varepsilon^{1/2}$ (the infinitesimal parameter). In this way the first contribution to the wave equation, which is the Laplacian operator in Eq. (25), will be of order ε . Assuming, for simplicity, a rotational symmetry around the propagation axis, the resulting correction to the KdV wave equation can be written as [44]

$$\left(s_t + \frac{\alpha}{2\rho c_0} s s_y + \beta s_{yyy} \right)_y = \frac{C_{\perp}}{2\rho c_0} \Delta_{\perp} s \quad , \quad (25)$$

where C_{\perp} is an elastic constant perpendicular to the direction of propagation. For a non-centrosymmetric crystal the right-hand side consists of two terms in the directions of the symmetry axes with their appropriate elastic constants. In the simulations of Sec. 3.2 and 3.3, along the c axis of sapphire, we will study the effect of the additional transverse gradients on the propagation of narrow strain beams.

3 Simulations

3.1 Soliton trains in sapphire

In this section we present numerical calculations of the nonlinear dispersive propagation of high-amplitude strain pulses in sapphire. It was discovered in the 60's by Zabusky and Kruskal [32] that the Korteweg-de Vries model is a nonlinear partial differential equation (PDE) that is integrable, meaning that analytical solutions can be obtained for any initial value or boundary condition imposed on the system. In practice, however, solutions can be written down in concise form only for the initial stage of development of the dispersive shock front and in the limit for

the soliton part of the wavepacket. The transition from the self-steepening regime to soliton trains, and the evolution of the rarefaction part of the wavepacket into an oscillating tail, can only be calculated numerically. The wave equation including damping, the KdV-Burgers equation, can also only be evaluated numerically. Therefore, we choose to compute the development of the initial pulse using numerical simulations of the KdV-Burgers equation.

The construction of a numerical solution for a nonlinear, dispersive wave equation with initial conditions is a specialized topic in itself. Especially the combination of a large nonlinear and small dispersive term poses strong demands on the stability of the numerical algorithm. Of the three approaches [45-47] that we have tested in the course of our investigations, the fastest, reasonably stable algorithm appeared to be the fourth-order Runge-Kutta scheme by Driscoll [46]. Its efficiency gain and method of implementation further allowed for a simple extension to the 2-dimensional problem of diffraction, which will be addressed in Sec 3.2.

	c_0 km/s	ρ kg/m ³	C_{33} GPa	α GPa	β 10 ⁻¹⁷ m ³ /s	ε (293 K) 10 ⁻⁴ Ns/m	C_{\perp} GPa
Al ₂ O ₃ [0001]	11.23	3.98	502	-1830	3.5	4.54	500

Table 1 Material parameters of *c*-axis sapphire relevant for the development of ultrashort acoustic soliton trains.

Using the one-dimensional wave equation Eq. (21), we have simulated the propagation of a typical experimental wavepacket over several millimeters in a sapphire (Al₂O₃) single-crystal. The transition from the shock-wave regime to soliton trains was studied by changing the damping parameter ε in the KdV-Burgers equation, between the value at room temperature and

the zero-damping limit. The material constants of the sapphire crystal along the crystallographic c direction [0001] are shown in Table 1.

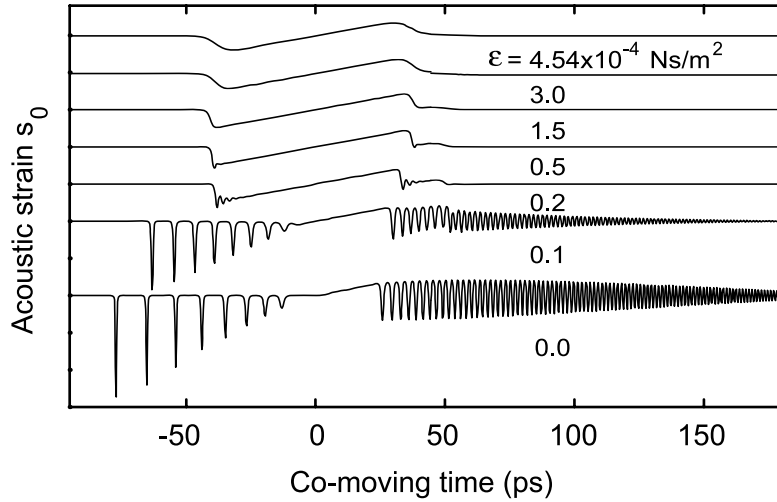


Figure 4 Strain waveforms after 1 mm propagated distance in sapphire [0001] for several values of viscosity parameter ε , calculated using the KdV-Burgers equation, Eq. (22) at a strain s_0 of 1.3×10^{-3} . The transition from shock waves to soliton trains takes place for a viscosity parameter between 2-5% of the room-temperature value.

Figure 4 shows the wavepacket developed after 1-mm of traveled distance through the sapphire, for an initial strain of 0.13% and for several values of the damping parameter ε . A value of 4.54×10^{-4} Ns/m corresponds to the viscosity of sapphire at room temperature [34]. We clearly observe the transition from an N-shaped shock wave at high viscosity values, via an oscillating shock front at around 2×10^{-5} Ns/m, to soliton train formation at a two times smaller value of ε . At a nonzero viscosity value, dissipation reduces the soliton pulse amplitudes as they propagate and thus leads to a slowing down of the shortest solitons, as can be seen by comparing the two

lowermost traces in Fig. 4. The bottom trace corresponds to the case of zero damping, where the solitons can propagate over long distances without distortion.

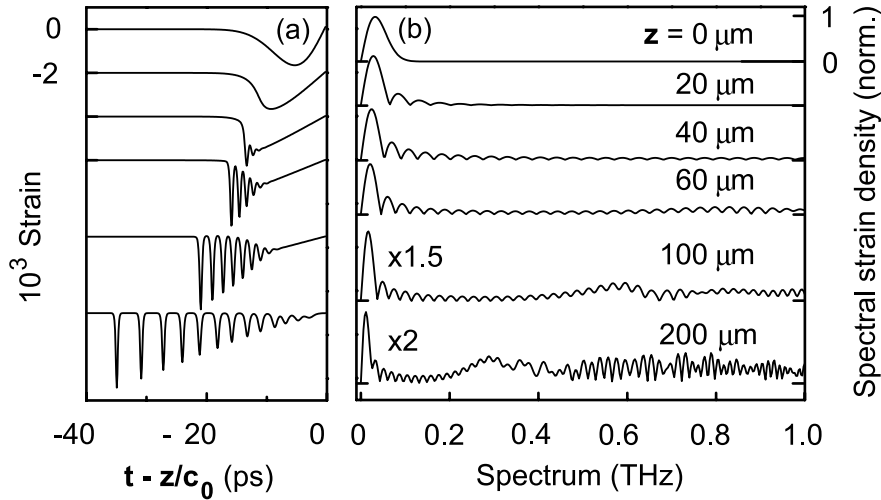


Figure 5 (a) Calculated development of the compressive part of the wavepacket using Eq. (21) with zero damping, for several propagation distances z . (b) Acoustic spectra corresponding to the development stages of (a), but for the complete bipolar wavepacket. Lower two spectra have been multiplied vertically for displaying convenience. (From Muskens, O.L., Dijkhuis, J.I, *Phys. Rev. B*, 70, 104301, 2004. With permission.)

The processes of self-steepening and subsequent breakup into soliton trains of the leading part of a typical strain pulse can be distinguished in Fig. 5(a). In the first 40 μm of the propagation distance the peak of the wavepacket shifts to the left, as its velocity is slightly higher than the linear sound velocity due to the local compression of the lattice. Figure 5(b) shows the frequency spectrum associated with the bipolar waveforms. We observe that the initial frequency spectrum below 100 GHz rapidly redistributes towards the higher harmonics and that the whole spectrum scales towards lower frequencies due to the expansion of the waveform. The strong upconversion

of strain, up to terahertz frequencies, is accompanied by a removal of energy from the lower-frequency part of the spectrum, an effect that we recognize in the experimental traces of Sec. 4. At the point where frequencies are high enough for dispersion to play a role [which effect in Eq. (21) is proportional to ω^3], the shock front starts to oscillate. Eventually the whole wave structure breaks up into a number of sharp peaked, half-cycle strain pulses, the acoustic solitons, with increasing amplitudes towards the front of the train. Concomitantly, as the soliton width and velocity scale with its amplitude, the leading soliton in the train is the fastest and the narrowest.

3.2 Diffraction and soliton train formation

In this section we investigate by a series of numerical simulations the influence of diffraction on the formation of acoustic solitons. We consider the typical conditions, met in our experiments and take sapphire as the material for our calculations. We assume cylindrical symmetry and a value of C_{\perp} of 500 GPa, which is a reasonable approximation around the c axis of sapphire. The ratio between nonlinearity and diffraction is varied by changing the transverse width of the Gaussian strain pencil launched into the material.

Diffraction has been included into the nonlinear wave motion by means of de Kadomtsev-Petviashvili equation [44], Eq. (25). The numerical algorithm used to calculate the propagation of a picosecond strain packet in a cylindrical geometry is an extension of the Runge-Kutta scheme of Sec. 3.1. Computational limitations restrict the calculations to strain amplitudes of 0.05% and to the first few hundred micrometers of propagation. This is sufficient to follow the

initial steps of the nonlinear evolution and the formation of a soliton train and to draw qualitative conclusions on the influence of diffraction.

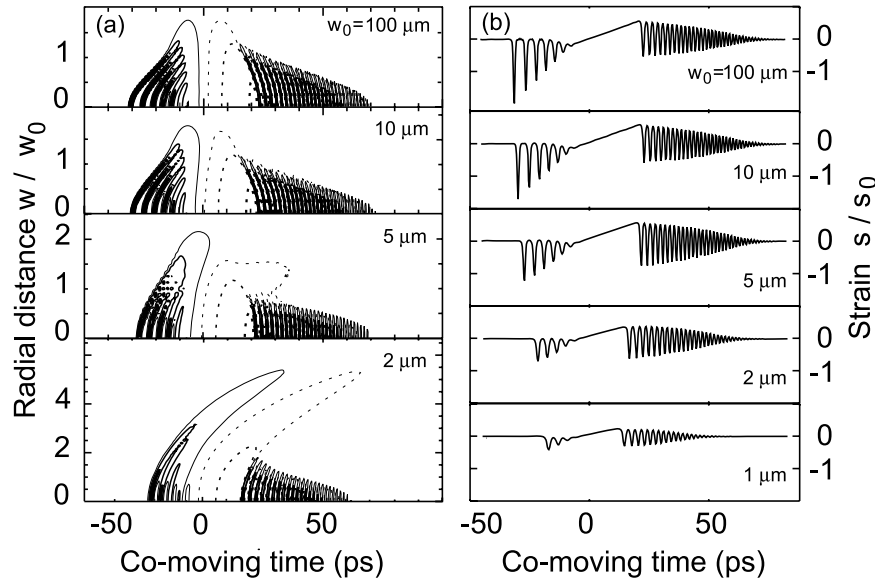


Figure 6 (a) Contour plots of the developed strain profiles after 1 mm in sapphire [0001], calculated for different transverse beam sizes w_0 , with a radial distance w normalized to w_0 . (Solid lines) denote negative strain contours, (dashed lines) denote positive strains. (b) Strain plots of the on-axis sections of (a), normalized to the initial strain s_0 of 0.05%.

We calculated the two-dimensional development of a cylindrical beam with a Gaussian radial intensity profile. Figure 6(a) shows radial profiles of the three-dimensional pulses after 0.45 mm of propagation, in the form of two-dimensional contour plots, for several diameters of the initial acoustic beam. The evolution of the profile with the largest beam waist of $100 \mu\text{m}$ [upper graph in Fig. 6(a)] is completely one-dimensional: diffraction plays no role. As usual, solitons appear at the front and a radiative tail is produced at the rear of the wavepacket, as is shown more clearly by the on-axis strain waveforms presented in Fig 6(b). The appearance of a positive curvature of

the solitons is due to the variation in strain amplitude over the profile, which translates directly into a velocity gradient by the properties of the KdV solitons.

For acoustic beam dimensions below 10 μm , an increasing influence of diffraction is observed. For these narrow beams, the transverse gradient of Eq. (25) results in a significant flow of energy out of the center of the acoustic beam. The nonlinear steepening process and concomitant breakup into solitons is severely frustrated by the reduction of the strain amplitude in the center of the beam. This can be most clearly seen in the on-axis curves presented in Fig 6(b). Clearly the number of solitons that develops from the initial packet decreases from 7 for the widest acoustic beams down to 3 for the narrow, 1- μm wide profile.

3.3 Stability of individual solitons

In the above simulations, the breakup into solitons of a micrometer-wide beam with frequency components around 30 GHz was shown to be strongly influenced by diffraction. In this section we will consider the diffraction of a single terahertz strain soliton. At a first glance, the development of a *single*, ultrafast strain soliton is expected to be less disturbed by diffraction. In the linear case, diffraction of a Gaussian beam is governed by the Fraunhofer formula [48]

$$w(z) = w_0 \left(1 + \left(\frac{c_0 z}{\pi v_{ph} (1 + 2p) w_0^2} \right)^2 \right)^{1/2} \quad (26)$$

where c_0 denotes the sound velocity, the acoustic frequency, and p is the phonon focusing parameter. For an initial frequency of 1 THz and an initial acoustic beam width of 10 micrometer, divergence is of order 10^{-4} , which is negligible over millimeter propagation

distances. Hao and Maris [26] used this linear diffraction argument to demonstrate that diffraction may be neglected in their soliton experiments. In the following, we will show that this assumption is not valid at all for nonlinear soliton beams.

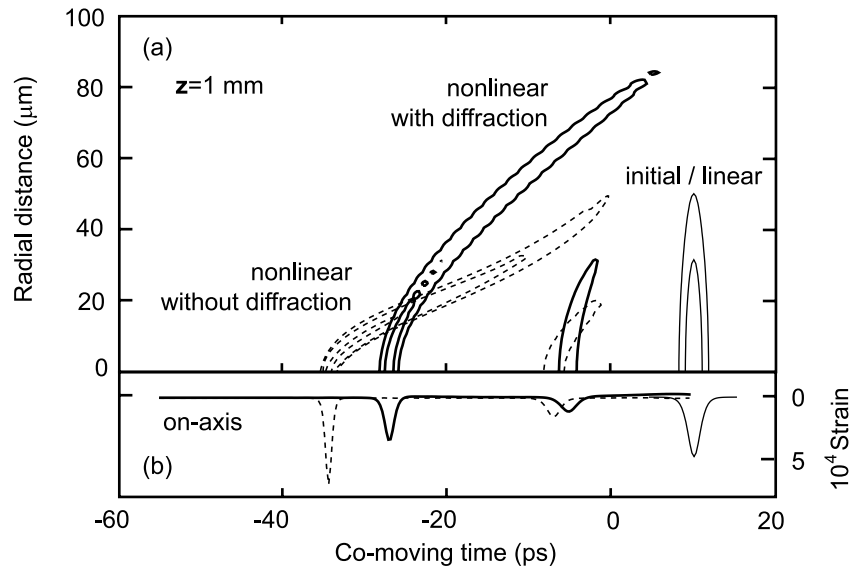


Fig. 7 (a) Radial profiles of an initial picosecond strain pulse (thin line, translated to 10 ps for displaying convenience), in sapphire [0001], in the cases of nonlinear propagation without diffraction (dashed line), and with diffraction (thick solid line). (b) On-axis strain waveforms of the profiles shown in (a).

The transverse gradient of Eq. (25), that is responsible for linear diffraction, results also in strong *nonlinear* distortion of the single, ultrashort solitons. This effect is illustrated by the calculations presented in Fig 7. Here, we calculate how a narrow cylindrical, high-amplitude wavepacket of 1 ps time duration breaks up into two soliton discs. The initial pulse, with a Gaussian transverse profile of 15 μm width [thin line in Fig. 7], is followed over 1 mm of propagation in sapphire.

We consider three different regimes of propagation: (i) linear propagation with diffraction, (ii) nonlinear propagation without diffraction, and (iii) nonlinear propagation with diffraction.

A low-amplitude pulse with this shape would not be influenced by diffraction, due to the high frequency content of the wavepacket [c.f. Eq. (26)]. The initial pulse [thin line in Fig. 7(a)] thus represents also the developed packet for situation (i). The one-dimensional, nonlinear propagation (ii) leads to a typical bell-shaped velocity profile (dashed line), that can be directly traced back to the initial Gaussian amplitude profile by the linear relation between amplitude and velocity of the KdV solitons. If finally dispersion is added to the nonlinear propagation, the profile changes significantly. Even for the relatively wide acoustic beam under study we observe a significant transverse spreading of the wavepacket (thick solid line), accompanied by a decrease of the on-axis soliton amplitude, as shown in Fig. 7(b).

From the above simulation we conclude that diffraction not only influences the self-steepening part of the wavepacket evolution, but also the propagation of single, three dimensional soliton objects, which are shown to be unstable in two dimensions. It is therefore impossible in this first-order framework to produce nanometer-sized solitary strain packets that are stable in all spatial dimensions.

4 Brillouin-scattering experiments

4.1 Introduction

In the previous sections we have shown that nonlinear elasticity theory combined with phonon dispersion predicts the formation of soliton trains from a high-amplitude, picosecond acoustic wavepacket. The experimental verification of this phenomenon is actually not straightforward. One has to be able to monitor the strain after large distances of propagation. The spatial dimensions of the solitons are much less than an optical wavelength, making direct observation only possible at sharp interfaces, e.g. at the surface of an opaque film. However, the requirement of a boundary layer prevents a continuous variation of the propagation distance, and interactions at the interface and material roughness may well disturb the soliton pulses before being detected. At much lower strain intensities, and concomitantly wider soliton pulses, it turned out already impossible to extract quantitative information from the reflectivity signal other than the propagation velocity [49]. As we anticipate ultrashort strain solitons of nanometer dimensions, surface detection is expected to become increasingly difficult.

An experimental technique which is well-suited to the detection of ultrashort strain solitons in *the bulk* of a crystal is Brillouin scattering. This method has a long history in the detection incoherent and thermal phonons, and allows for a sensitive determination of acoustic-phonon sound velocities in crystals. Only very recently, its use has been demonstrated in the field of coherent phonons and picosecond acoustic wavepackets [48,50-52]. As the light scattered from the propagating acoustic waves undergoes a frequency shift corresponding to the absorbed phonon energy, signals can be easily filtered using multipass interferometry. Furthermore, its selectiveness for the momentum ensures that only the directional phonon wavevectors matching with the scattering angle can be selected. In this way, Brillouin spectroscopy yields important

information on the development of the gigahertz frequency spectrum of the acoustic wavepackets.

We have chosen to use the spectrometer as a local probe of strain components, by focusing the probe laser tightly through the side windows of an optical cryostat in which the sample is immersed and collecting the directional beam of scattered light. In this way we can obtain information on the development of individual spectral components as the acoustic wavepacket propagates over millimeter distances through the crystal. As we will show below, this method yields typical patterns in the distance-dependence of the scattered intensity that demonstrate the transition from the shock wave regime to soliton trains.

4.2 Setup

For the propagation experiments we use a piece of high-quality (< 1 ppm. impurity ions) single-crystal sapphire of $5 \times 11 \times 10$ -mm³ dimensions, with the c -axis aligned perpendicular to the 5×11 -mm² surface, covered with a 100-nm thin chromium transducer. The crystal is mounted into an optical cryostat to perform experiments down to liquid helium temperatures. Strain wavepackets of very short (picosecond) time duration are generated using the conventional method of ultrafast heating of the chromium film that is evaporated onto the sapphire crystal. It is well-known that chromium has a very high electron-phonon coupling constant of 420×10^{15} W/m³ K, and thus the electronic excitation is converted to a coherent strain over a distance of the order of the optical absorption length. Acoustic strain pulses in the high-amplitude regime are generated using an amplified Ti:sapphire laser setup, which provides 130-fs laser pulses at 800 nm with an energy of

0.7 mJ/pulse, at a repetition rate of 1.0 kHz. To obtain excitation over a large area, the output of this laser is weakly focused to a spot of several millimeters in diameter onto the sample. The optical pump fluence is varied by controlling the position of this focusing lens, the upper limit being the damage threshold of our transducer at 15 mJ/cm^2 . Small-area, low-amplitude acoustic pulses can be generated as well, using the mode-locked output of the Ti-sapphire laser system, carrying 7 nJ pulses at a repetition rate of 80 MHz.

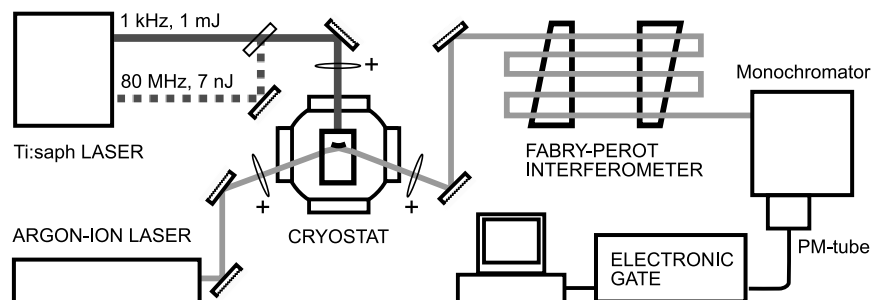


Figure 8 Brillouin scattering setup for the generation and detection of high-amplitude acoustic wavepackets in a transparent crystal.

Figure 3 shows the experimental configuration for the scattering experiment. The optical probe is a single-mode argon-ion laser operating at 514.5 nm and delivering 60 mW of optical output power. The optical beam is tightly focused inside the crystal to a waist of several micrometers. The frequency-shifted scattered radiation is analyzed by a quintuple-pass Fabry-Pérot interferometer (Burleigh RC110) and detected using standard photon counting techniques. The same spectrometer setup has been used earlier to study the propagation of coherent, monochromatic phonon beams and of ultrashort strain pulses in lead molybdate and paratellurite [48,50-52].

4.3 Transition from Shock Waves to Soliton Trains

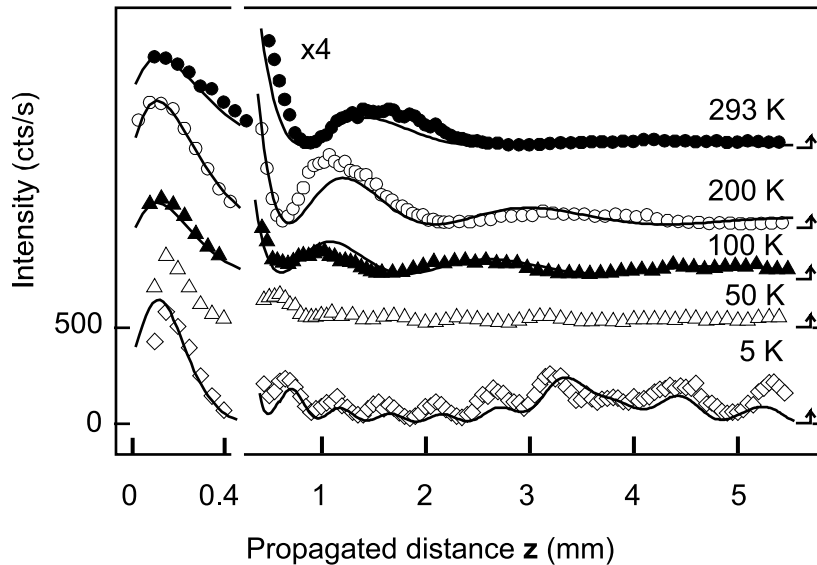


Figure 9 Brillouin scattering intensity at 22 GHz as a function of propagated distance in sapphire [0001], for several temperatures between 293 K and 5 K. Symbols indicate experimental data, lines simulation results for the KdV-Burgers model, Eq. (21). (From Muskens, O.L., Dijkhuis, J.I, *Phys. Rev. Lett.*, 89, 285504, 2002. With permission.)

By measuring the Brillouin scattering intensity in the crystal as a function of distance from the transducer, we monitor one single Fourier-component of the strain wavepacket. Figure 9 shows this development at an acoustic frequency of 22 GHz, for five values of the sample temperatures. Generally, the shape of the traces consists of two distinct parts: (i) within the first hundreds of micrometers, the Brillouin intensity drops dramatically by almost an order of magnitude, followed by (ii) oscillations of the intensity as a function of propagated distance. Feature (i) does not seem to depend strongly on the temperature, be it that the decay speeds up slightly towards

lower temperatures. However, the oscillations of (ii) show a pronounced, qualitative change in behavior below a certain critical point, at a temperature between 50 K and 100 K. Above this critical temperature, only a few oscillations take place in the propagation length of about 6 mm, with a period that grows longer upon propagation in the crystal.

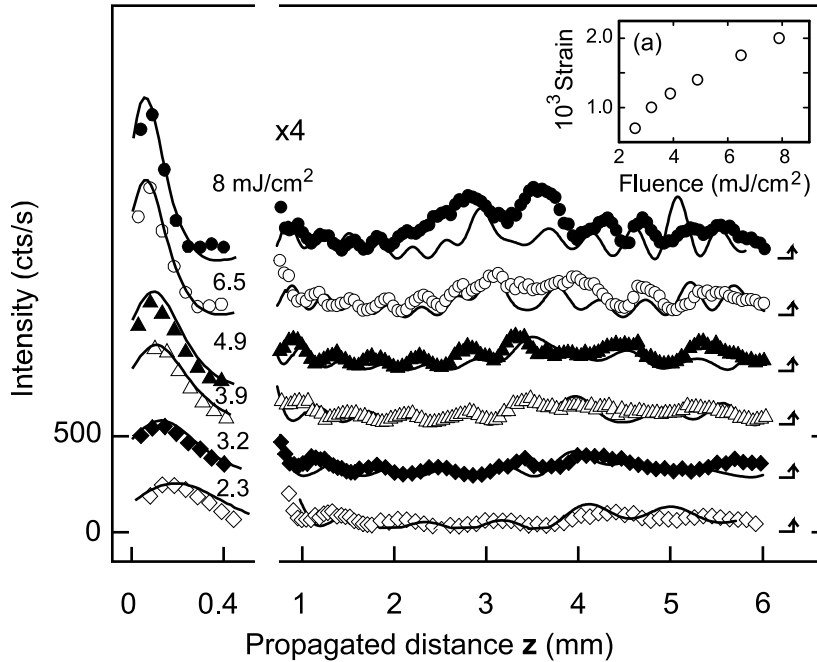


Figure 10 Brillouin scattering intensity at 22 GHz against propagation distance for several values of pump fluence E , at a temperature of 5 K. Symbols indicate experimental data, lines simulations using the KdV model, Eq. (15). (From Muskens, O.L., Dijkhuis, J.I., *Phys. Rev. Lett.*, 89, 285504, 2002. With permission.)

Below the critical temperature, however, we clearly observe a large number of oscillations with a period that remains constant over the long travel distances of several millimeters. After a distance of several millimeters in the crystal, the patterns become more intricate and can no longer be interpreted as a single oscillation. This behavior of the scattering intensity at the

lowest temperature is studied further as a function of the pumping power of the femtosecond laser. These low-temperature data, shown in Fig. 10, clearly demonstrate that the oscillations in the Brillouin traces become faster with increasing pump fluence.

At this point there are two ways to compare these data with theory: either direct comparison with numerical simulations of the nonlinear wavepacket evolution or analysis of the oscillation frequencies followed by comparison with analytical expressions to recover the essential soliton parameters.

Reproduction of the experimental data by numerical calculations using the KdV-Burgers equations can be performed over all ranges of strain amplitudes and temperatures under study, as was shown in Ref. [1]. Together with independent estimates of the initial wavepacket shape from time-resolved experiments [2] and the known material parameters of sapphire (see Table 1), we calculated the nonlinear evolution of the pulse over millimeter distances using the numerical schemes of Sec. 3. To arrive at the simulated Brillouin traces, we Fourier-transformed the time-domain simulations of the wavepacket taken at discrete distances z , and took the square of the resulting spectral component at the Brillouin frequency. The resulting curves as a function of propagated distance z are plotted as the lines in Figs. 9 and 10. We observe excellent agreement with the experimental data points for realistic values of acoustic strain s_0 [see Fig. 10(a)] and the viscosity parameter ε [see Fig. 4].

The features observed in the Brillouin data can now be traced back via the simulations to the time-domain evolution of the wavepacket. For example, the decay of the Brillouin scattering intensity within the first hundred micrometers is the signature for self-steepening of the acoustic wavepacket. Figure 5 showed that the formation of a sharp shock front is accompanied by the

formation of many higher harmonics of the fundamental frequency of the bipolar waveform. This redistribution of energy over a spectral window as large as 1 THz inevitably leads to a reduction in amplitude of the lower, GHz strain components that are detected with the Brillouin scattering method.

Subsequently, the spreading of the wavepacket results in a drift of the spectral characteristics towards lower frequencies. As the packet broadens on its journey through the crystal, the harmonic peaks are transported towards the GHz frequency-range, where they are detected as oscillations in the scattered intensity traces of Figs. 9 and 10. The transition from slow to fast oscillations at a critical temperature in the traces of Fig. 9 can be explained by the dynamics of the wavepacket spreading, that behaves diffusively (i.e. proportional to $z^{1/2}$) in the case of viscously damped N-waves (c.f. Sec. 2.4) and goes with a constant velocity for soliton trains (c.f. Sec. 2.3).

We conclude that the measured Brillouin intensity can be explained well using numerical simulations based on solving the KdV-Burgers equation. We now arrive at the second approach, namely the explanation of our low-temperature data using exclusively the analytical KdV framework of Sec. 2.3. In this method we interpret the Brillouin scattering intensity in terms of spatial resonance and Bragg reflections of the light scattered from the moving soliton train. This approach was worked out into detail in Ref. [2].

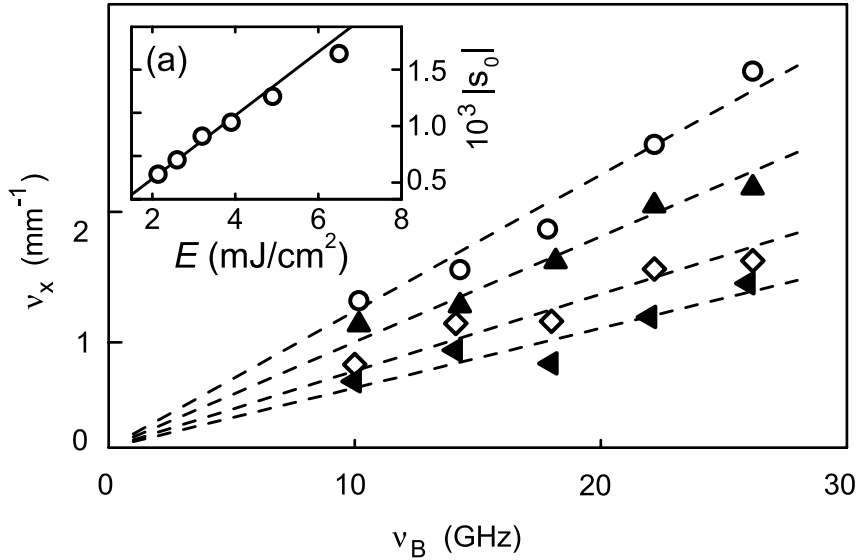


Figure 11 Maximum spatial frequencies ν_x determined from Brillouin traces at frequencies ν_B , for several values of pump fluence E . Lines (dash) denote fits using Eq. (27). (a) Initial strain values s_0 obtained from fitting the experimental data. (From Muskens, O.L., Dijkhuis, J.I, *Phys. Rev. B*, 70, 104301, 2004. With permission.)

The Brillouin intensity plots of Fig. 10 consist of an intricate pattern that can be unraveled by performing a spatial Fourier transform of the experimental traces. The highest frequencies in the pattern are due the characteristic oscillations during the first millimeters. By counting the number of these oscillations per mm, we can determine the typical frequency contained in the oscillation pattern. This quantity, which we will denote as the spatial beating frequency ν_x , can be

determined for traces at different pump intensities and for different scattering angles. These two degrees of freedom yield a complete picture of the behavior of ν_x , as can be shown in Fig 11.

This figure shows the dependence of the typical beating frequency on the selected Brillouin frequency ν_B , for some selected pump intensities E . We observe a clear relation between the oscillation frequency in the scattering pattern and the frequency of the selected Brillouin

component. The dependence is approximately linear, with a slope increasing with pump fluence. This slope can be used to derive information on the velocities and amplitudes of the strain solitons, as we show below.

The presence of oscillations in the Brillouin scattering traces can be explained quantitatively by a simple model based on optical interference of solitons moving at different velocities [2]. It can be easily deduced that two objects moving with a velocity difference Δc in the moving frame system produce a beating in the scattered intensity against distance with a spatial frequency given by

$$v_x = \frac{\Delta c v_B}{c_0^2}. \quad (27)$$

The dependence of v_x on the Brillouin frequency in Eq. (27) agrees well with that observed in Fig. 11 and we can fit the experimental data to obtain values for the velocity difference Δc . Considering that the highest beating frequency is produced by the interference of the fastest solitons and the linear parts of the wavepacket, the expressions relating velocity and amplitude derived below Eq. (19) can be used to link these velocity differences to the soliton amplitude, which for sapphire gives $\Delta c/c_0 = 0.61|a_1|$. Using further that the amplitude of the first soliton a_1 is two times that of the initial strain pulse s_0 [c.f. Eq. (20)], we can deduce the strain from the slopes of Fig. 11. The resulting values for s_0 obtained from the fits at different pump fluences are shown in Fig. 11(a) and show good agreement with those values obtained from direct numerical reproduction of the Brillouin traces at 22 GHz [c.f. Fig. 10(a)].

4.4 Diffraction and the formation of solitons

In the above discussion, we have considered the nonlinear propagation of millimeter-wide, nanometer thick acoustic discs. The simulations of Chapter 3 predicted negligible diffraction under these conditions. This situation changes as soon as the initial acoustic beam width becomes of the order of several micrometers. We have attempted to investigate experimentally the propagation of an initially narrow strain profile. For this purpose, we focused down the ultrafast pump laser to a measured waist of 12 μm . We have chosen to study a different system, namely lead molybdate [001] covered with a gold transducer, mainly because of the superior acousto-optic properties of the lead molybdate compared to the sapphire used in the one-dimensional experiments.

The sample is a $9 \times 11 \times 10\text{-mm}^3$ crystal of lead molybdate (PbMoO_4), with the [001]-direction aligned perpendicular to the $9 \times 11\text{-mm}^2$ surface. A 500-nm gold film is deposited onto this surface. Small-area, low-amplitude acoustic pulses can be generated using the mode-locked output of the system [‘oscillator’ in Figs. 12 and 13], carrying 7 nJ/pulse at a repetition rate of 80 MHz. The amplified laser pulses can also be focused to the same 12- μm waist after severe attenuation, to study the regime of high-intensity, small-area excitation.

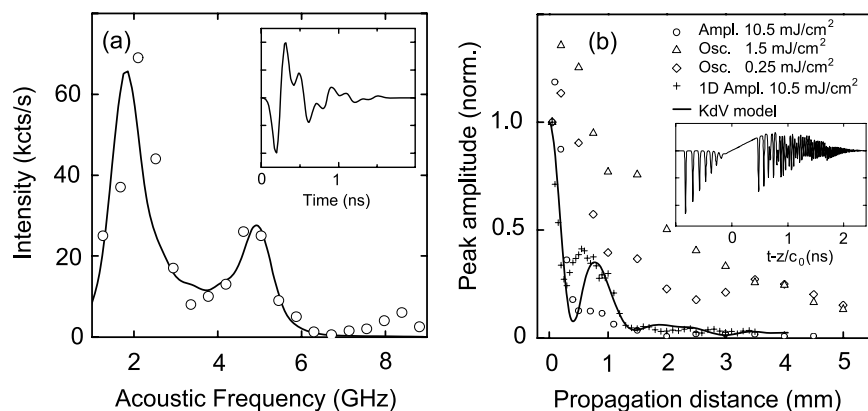


Figure 12 (a) Acoustic power spectrum of a strain packet generated in a gold film with a 70-cm chromium overlayer. (o) denotes experimental points, line is fit using the wavepacket shown in (inset). (b) Peak amplitude of the small-area (12- μm wide) strain pencils against propagated distance in the lead molybdate crystal, both for high-power (‘amplifier’) and low-power (‘oscillator’) excitation, together with an evolution trace of a large-area acoustic beam at high power. (Inset) shows developed wavepacket corresponding to the 1D-fit (line) in (b).

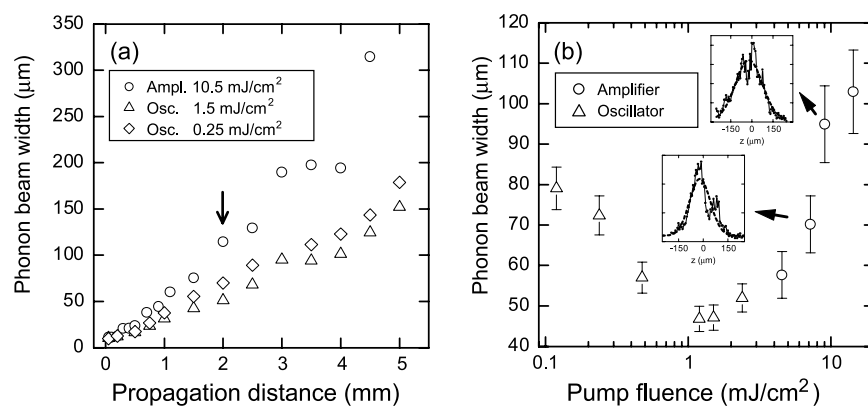


Figure 13 (a) Acoustic beam 1/e halfwidth against propagated distance for the three pump fluences 0.25, 1.5, and 10.5 mJ/cm². Arrow denotes position where the dependence of (b) is determined. (b) Phonon beam width against pump fluence at $z = 2$ mm. (Insets) typical transverse scans of the profile at high pump fluences.

Figure 12 (a) shows a typical power spectrum of the initial acoustic wave packet in the crystal, after a 100- μm traveling distance. The spectrum can be fitted with a bipolar waveform consisting of multiple reflections of 45% from the gold-lead molybdate interface. The large temporal width of the pulses implies that soliton-formation will only start up after a significant amount of self-steepening of the packet has taken place. In the following we will concentrate on a single frequency-component of the wave packet, which we have chosen to be the sub-maximum at 5 GHz. The propagation and diffraction of this component for a small-area initial packet was followed through the crystal at three settings of the pump-laser fluence, covering the entire dynamic range of our experiment. The peak amplitude in the center of the acoustic beam and the width of the strain profiles are shown in Fig. 12 (b) and Fig. 13 (a), respectively. At the highest pump fluence under study, the evolution of a large-area, nondiffracting packet was also measured for comparison. From the figures, we can observe a significant difference in evolution at the three pump fluences under study. We know from simulations based upon the KdV-equation that, in absence of diffraction, the initial decay of the power at low frequencies can be attributed to self-steepening of the wave packet [3]. Comparison of the two traces at 10 mJ/cm^2 shows, for both, a fast decrease of peak intensity, but for the ‘small-area’ trace followed by an oscillation of lower amplitude than in the ‘large-area’ curve. The decrease of the amplitude of oscillation makes us believe that part of the initial spectral power is diffracting away from the central part of the beam. Evidence of this can also be found in Fig. 13 (a). We observe an increase in beam-width of almost an order of magnitude within the first millimeters of propagation. Further, the diffraction is observed to depend on pump fluence. This point is investigated further in Fig. 13 (b), which shows the dependence of the beam width after 2 mm

propagated distance against pump fluence. Clearly the behavior can be separated into two regimes of decreasing and increasing beam divergence, respectively, with increasing pump fluence. The two regimes are distinguished by a minimum in beam divergence found at a fluence of 1.5 mJ/cm^2 . At the highest intensities, we have further observed structures of smaller dimensions inside the broad ‘envelope’ [insets of Fig. 13 (right)], which indicate that the profiles consist of different contributions in the radial distribution of the wave packet.

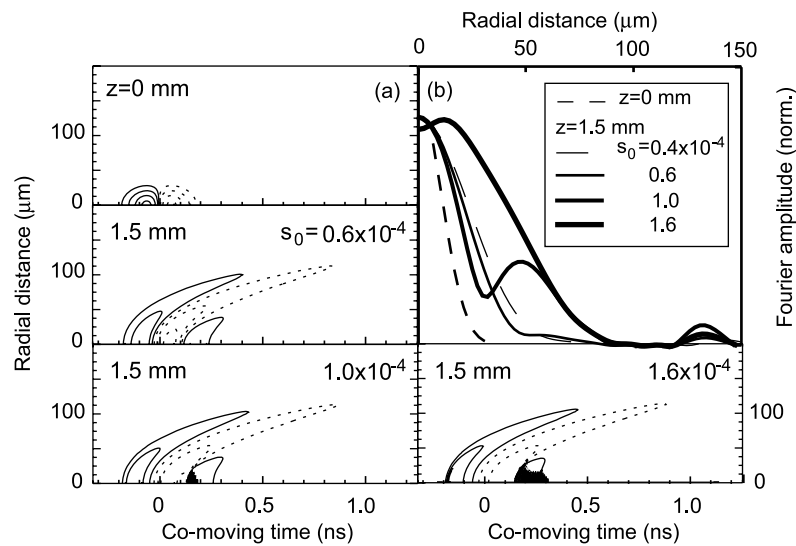


Figure 14 Calculated diffraction of an acoustic wavepacket in lead molybdate [001] after 1.5 mm of propagation. (a) Radial profiles of the strain waveforms, (solid lines) denote negative strain contours, (dashed lines) denote positive strains. (b) Absolute Fourier component at 5 GHz of the wavepackets of (a) against radial distance.

The behavior of Fig. 13(b) can be explained qualitatively by the influence of nonlinear propagation of the total packet on the diffraction of individual frequency components. As we will show below, two regimes can be identified, namely (i) suppression of diffraction due to self-steepening and frequency upconversion, and (ii) defocusing of nonlinear shock fronts and the

solitons. This is made clear by a series of simulations presented in Fig. 14, showing the calculated propagation of a typical initial wave packet [upper graph, Fig. 14(a)] that is consistent with the observed frequency spectrum in lead molybdate. We used the estimated values of the acoustic nonlinearity and phonon dispersion for lead molybdate estimated in Ref. [51].

Simulations were limited to a maximum traveling distance of 1.5 mm and to an initial beam profile of 15 μm halfwidth. However, qualitatively the results can be compared well to the above diffraction experiment.

Figure 14(a) shows the developed state of the two-dimensional wave packet, for three values of the initial acoustic strain s_0 . Transverse profiles of the spectral strain component at 5 GHz were obtained from the time-domain data by performing Fourier transforms at each radial distance. The resulting profiles, shown in Fig. 14(b), demonstrate that the radial distribution of individual strain components depends strongly on the nonlinear propagation of the total wave packet. The profile at the lowest strain amplitude corresponds to the form obtained by linear Fraunhofer diffraction of the 5 GHz component [c.f. Eq. (26)] and shows a factor two increase in beam width relative to the initial profile. With increasing strain amplitude we find initially a *decrease* of the beam width. However, at slightly higher strain values a strong *increase* of the profile width appears. This increase of the width is accompanied with a typical oscillating structure in the transverse profile that resembles the observed behavior at the highest pump fluences in Fig. 13(b).

Comparison with the corresponding time-domain traces of Fig 14(a) relates the behavior to the different stages in nonlinear and dispersive development of the wave packet. The two lowest

strain values, that showed the reduction of divergence with strain amplitude, differ only in the amount of self-steepening. At these intensities, no dispersive features like solitons and an oscillating tail have yet developed. We therefore conclude that self-steepening leads to a reduction of the beam divergence.

In the simulations at higher strain amplitudes, we do observe signatures of dispersive development. An oscillating tail emerges and we can even distinguish one or two solitons separating at the front. The Fourier-transform profiles taken from these simulations show a broadening of the beam width and the appearance of some structure in the transverse profile. We conclude thus that the combined nonlinear dispersive behavior is accompanied by an enhanced divergence of the acoustic beam.

These simulation results can be understood more intuitively from the behavior of Eq. (25). At moderate strain amplitudes, the initial effect of nonlinearity is to weakly couple the spectral modes of the strain wavepacket. A mutual up- and downconversion of frequency components is responsible for self-steepening and the generation of higher harmonics, as was observed in the one-dimensional simulations of Fig. 5. As the higher frequencies diffract less, the divergence of lower frequency components will also be reduced due to the nonlinear coupling of modes. At higher strain amplitudes, the appearance of appreciable nonlinear velocity differences and break up into dispersive structures will result in the conversion of amplitude variations into a velocity profile, resulting in an enhanced (positive) curvature of the wavefront. The concomitant appearance of strong transverse gradients then results in a flow of energy from the center of the acoustic beam towards the edges of the profile, as was observed in the simulations of Sec. 3.2.

The presented work gives a qualitative idea of the influence of nonlinearity and dispersion on the diffraction of a narrow strain beam. On the other hand, the simulations presented in Sec. 3.2 have explored the influence of diffraction of the soliton development. The two together provide a first impression on the stability of nonlinear waves against transverse disturbances. This could be of key importance for future applications of nano-ultrasonic waves in imaging and manipulating of condensed matter. More detailed experimental verification of these complex interactions, achievable for example using time-resolved two-dimensional imaging, will have to be performed to get a deeper insight in the development of acoustic solitons in more dimensions.

5 Conclusions and Prospects

We have investigated, both theoretically and experimentally, the nonlinear development of high-intensity acoustic pulses through a single crystal of macroscopic dimensions. Brillouin spectroscopy turned out to be a useful technique for studying shock wave and soliton development in the bulk of a transparent crystal. We used the decay of the scattered intensity as a signature of self steepening and analyzed the subsequent oscillation pattern in terms of spatial resonances of a moving soliton train. The spatial beating frequencies found in the oscillation pattern can be used as a measure for the different velocities in the train, that translate directly into estimates for the number and width of the solitons using either numerical simulations or the analytical framework of the Korteweg-de Vries model.

Further we have explored the influence of diffraction on the nonlinear development of a narrow strain pencil. Comparison with simulations shows that self-steepening tends to decrease divergence due to the formation of nondiffracting, higher frequency components. However, as the wavefronts curve due to the nonlinear velocity difference between the center and exterior regions of the beam, the influence of diffraction on the nonlinear solitons is enhanced. This effect results in a transverse instability and eventual the decay of narrow soliton discs upon propagation in the crystal.

One might argue for another application of Brillouin scattering in the analysis of soliton trains. In principle it would be possible to determine the different velocities in the wavepacket directly from the frequency shifts of the light scattered from the individual solitons. For the backscattering condition this shift amounts to several GHz for the typical solitons found in this chapter. The condition for spectral separation of the backscattered radiation for each *individual* soliton can be easily fulfilled by the spectral resolution of our interferometer. This allows in principle the detection of the Brillouin peaks for the individual solitons in the train. The detection of these individual soliton contributions will be a topic of future experiments.

At this point we wish to speculate about some possible new avenues and perhaps applications for ultrafast high-amplitude strain pulses in solids.

Of course, one can ask the question if transverse soliton trains are feasible to generate. One possibility perhaps is to inject the strain pulses at an angle to the symmetry axis of the crystal. This will lead to both longitudinal and transverse components of the injected strain packets that

will quickly separate during propagation and may develop into trains of longitudinal and transverse solitons. Alternatively, one can think of mode-converting a developed longitudinal soliton train by reflection at a surface and choosing a suitable angle between the soliton beam and the normal to the surface.

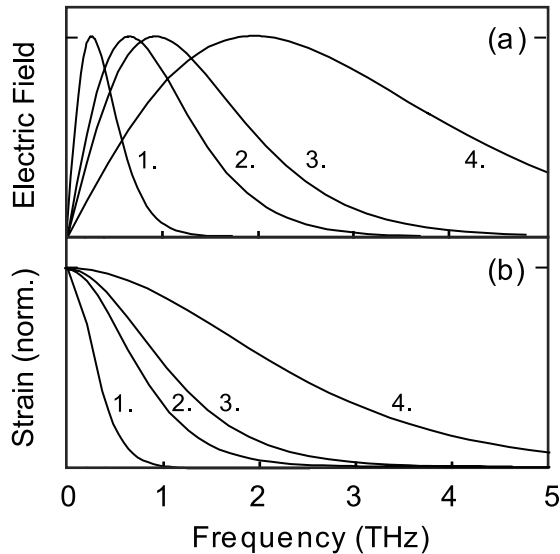


Figure 15 (a) Predicted terahertz electromagnetic spectrum from the reflection of a single strain soliton at a piezoelectric interface, calculated for the four substrate materials of (b). (b)

Calculated single-soliton spectra for 0.4% strain solitons generated in 1. Silicon [100], 2. Quartz [0001], 3. Sapphire [0001], and 4. MgO [100].

Another promising direction could be to generate terahertz solitons in piezoelectric crystals and convert them by reflection at a crystal surface into intense electromagnetic terahertz pulses.

Figure 15 shows the typical terahertz electromagnetic spectrum that could be obtained using the strain solitons formed in some typical materials. These terahertz electric fields should be detectable by electro-optic sampling. Conversion of ultrasound into microwaves is well known in the field of ultrasonics, but is never demonstrated in the terahertz regime simply because

coherent terahertz sound waves were not available until now. At one hand such schemes may allow for a direct analysis of the time-dependent strain in the soliton train and at the other hand permit the generation of strong terahertz fields at surfaces that can be instrumental to study electrons in nanostructures on surfaces, or perhaps to address elements in micro-photonic devices.

A quite fundamental question is to what extent a strain solitons in a resonant medium can transform to a resonant soliton. From soliton experiments in optically excited ruby it appeared that the coupling is strong enough that the typical Bloch angle for the $2\bar{A}({}^2E) \rightarrow \bar{E}({}^2E)$ phonon transition at 870 GHz reaches values of a few degrees [3]. In case the two-level systems are prepared inverted, coherent amplification will take place, like in an laser amplifier, and the Bloch angle may exponentially grow until angles exceeding π are reached and stable resonant 2π -solitons may be formed. Here one could create a *soliton phonon laser* at terahertz frequencies. Such pulses can be used to study *self-induced transparency* of phonons or to produce *phonon echoes* in resonant media. Again such phenomena are already demonstrated in ultrasonic experiments at microwave frequencies but are never shown in the terahertz domain.

A fundamental limit of soliton propagation can be reached in materials with a low sound velocity, like lead molybdate: here it is possible to create solitons with a width approaching the lattice constant [52]. As a result dispersion becomes particularly large and the description in terms of discrete lattice model becomes a prerequisite.

Finally, it is of interest to devise schemes in which the soliton reaches pressures close to the internal pressure of the crystal and study properties of matter under extreme conditions and create *nano-explosions*. Thanks to the high-frequency content of the soliton pulses focusing strain pulses to extremely small spots may be possible. To examine these effects, it is relevant to study the nonlinear propagation of spherical wave fronts employing the numerical techniques described in this chapter to see to what extent geometrical focusing can enhance the strains in the pulses to the desired levels. Experimentally, spherical wave fronts can be generated by evaporating the transducer on a surface of the crystal that is prepared with a spherical shape.

We expect high-amplitude nano-ultrasonics to develop further into the direction of technological applications. Possibly the concept of ultrashort strain solitons will play an important role in this. The ability to convert energy from an initially broad packet into sharp, localized pulses is a unique feature that may find its way into manipulation and characterization of condensed matter. The feasibility to generate soliton pulses up to more elevated temperatures will certainly increase the range of potential applications in science and technology.

The authors wish to thank P. Jurrius and C. R. de Kok for their technical assistance. This work was supported by the Netherlands Foundation "Fundamenteel Onderzoek der Materie (FOM)" and the "Nederlandse Organisatie voor Wetenschappelijk Onderzoek (NWO)."

References

[1] Muskens, O.L. and Dijkhuis, J.I., High amplitude, ultrashort, longitudinal strain solitons in sapphire, *Phys. Rev. Lett.*, 89, 285504, 2002.

- [2] Muskens, O.L. and Dijkhuis, J.I., Inelastic light scattering by trains of ultrashort acoustic solitons in sapphire, *Phys. Rev. B*, 70, 104301, 2004.
- [3] Muskens, O.L., Akimov, A.V., and Dijkhuis, J.I., Coherent interactions of terahertz strain solitons and electronic two-level systems in photoexcited ruby, *Phys. Rev. Lett.*, 92, 335503, 2004.
- [4] Tucker, J.W. and Rampton, V.W., *Microwave Ultrasonics in Solid State Physics*, 1st ed., Elsevier, New York, 1972.
- [5] Grill, W. and Weis, O., Excitation of coherent and incoherent terahertz phonon pulse in quartz using infrared laser radiation, *Phys. Rev. Lett.*, 35, 588, 1975.
- [6] Shiren, N.S., Measurement of signal velocity in a region of resonant absorption by ultrasonic paramagnetic resonance, *Phys. Rev.*, 128, 2103, 1962.
- [7] Jacobsen, E.H. and Stevens, K.W.H., Interaction of ultrasonic waves with electron spins, *Phys. Rev.*, 129, 2036, 1963.
- [8] Tucker, E.B., Amplification of 9.3-kMc/sec ultrasonic pulses by maser action in ruby, *Phys. Rev. Lett.*, 6, 547, 1961.
- [9] Bron, W.E. and Grill, W., Stimulated phonon emission, *Phys. Rev. Lett.*, 40, 1459, 1978.
- [10] Hu, P., Stimulated emission of 29 cm^{-1} phonons in ruby, *Phys. Rev. Lett.*, 44, 417, 1980.
- [11] Sox, D.J., Rives, J.E., and Meltzer, R.S., Stimulated emission of 0.2-THz phonons in $\text{LaF}_3:\text{Er}^{3+}$, *Phys Rev. B*, 25, 5064, 1982.
- [12] Van Miltenburg, J.G.M. et al., Stimulated emission and decay of phonons resonant between the Zeeman states of $E({}^2E)$ in ruby, in *Phonon Scattering in Condensed Matter*, Eisenmenger, W., Laßman, K., and Döttinger, S., Eds., Springer, New York 1984, p. 130.

- [13] Overwijk, M.H.F., Dijkhuis, J.I., and De Wijn, H.W., Superfluorescence and amplified spontaneous emission of 29-cm^{-1} phonons in ruby, *Phys. Rev. Lett.*, 65, 2015, 1990.
- [14] Thomsen, C. et al., Coherent phonon generation and detection by picosecond light pulses, *Phys. Rev. Lett.*, 53, 989, 1984; Surface generation and detection of phonons by picosecond light pulses, *Phys. Rev. B*, 34, 4129, 1986.
- [15] Wright, O.B. and Kawashima, K., Coherent phonon detection from ultrafast surface vibration, *Phys. Rev. Lett.*, 69, 1668, 1992.
- [16] Bosco, C.A.C., Azevedo, A., and Acioli, L.H., Laser-wavelength dependence of the picosecond ultrasonic response of a NiFe/NiO/Si structure, *Phys. Rev. B*, 66, 125456, 2002.
- [17] Baumberg, J.J., Williams, D.A., and Köhler, K., Ultrafast acoustic phonon ballistics in semiconductor heterostructures, *Phys. Rev. Lett.*, 78, 3908, 1997.
- [18] Wright, O.B. et al., Ultrafast carrier diffusion in gallium arsenide probed with picosecond acoustic pulses, *Phys. Rev. B*, 64, 081202, 2001.
- [19] Yahng, J.S. et al., Probing strained InGaN/GaN nanostructures with ultrashort acoustic phonon wave packets generated by femtosecond lasers, *Appl. Phys. Lett.*, 80, 5223, 2002.
- [20] Sugawara, Y., et al., Watching ripples on crystals *Phys. Rev. Lett.*, 88, 185504, 2002.
- [21] Vertikov, A., et al., Time-resolved pump-probe experiment with subwavelength lateral resolution, *Appl. Phys. Lett.* 69, 2465, 1996.
- [22] Duquesne, J.-Y. and Perrin, B., Ultrasonic attenuation in a quasicrystal studied by picosecond acoustics as a function of temperature and frequency, *Phys. Rev. B*, 68, 134205, 2003
- [23] Daly, B.C. et al. Imaging nanostructures with coherent phonon pulses, *Appl. Phys. Lett.*, 84, 5180, 2004.

- [24] Hao, H.-Y. and Maris, H.J., Study of phonon dispersion in silicon and germanium at long wavelengths using picosecond ultrasonics, *Phys. Rev. Lett.*, 84, 5556, 2000.
- [25] Hao, H.-Y. and Maris, H.J., Dispersion of the long-wavelength phonons in Ge, Si, GaAs, quartz and sapphire, *Phys. Rev. B*, 63, 224301, 2001.
- [26] Hao, H.-Y. and Maris, H.J., Experiments with acoustic solitons in crystalline solids, *Phys. Rev. B*, 64, 064302, 2001.
- [27] Bradley, C.C., *High pressure Methods in Solid State Research*, 1st ed. Plenum Press, New York, 1969
- [28] Trunin, R. F., *Shock Compression of Condensed Materials*, 1st ed. Cambridge University Press, Cambridge, 1998.
- [29] Love, A.E.H., *Treatise on the Mathematical Theory of Elasticity.*, 1st ed. Cambridge University Press, Cambridge, 1937.
- [30] Murnaghan, F.D., *Finite Deformations of an Elastic Solid*, 1st ed., John Wiley & Sons, New York, 1951.
- [31] Korteweg, D.J. and de Vries, G., On the change of form of long waves advancing in a rectangular canal, and on a New Type of Long Stationary Waves, *Philos. Mag.* 39, 422, 1895.
- [32] Zabusky, N.J. and Kruskal, M.D., Interaction of "solitons" in a collisionless plasma and the recurrence of initial states, *Phys. Rev. Lett.*, 15, 240, 1963.
- [33] Wallace, D.C., in *Solid State Physics*, Ehrenreich, H., Seitz, F., and Turnbull, D., Eds., Academic, New York, Vol. 25, p. 301, 1970.
- [34] Auld, B.A., *Acoustic Fields and Waves in Solids*, vol. 1., 2nd ed., Robert E. Krieger Publishing Company, Malabar, FL, 1990.
- [35] Kittel, C., *Introduction to Solid State Physics*, 6th ed., John Wiley & Sons, New York, 1986.

- [36] Whitham, G.B., *Linear and Nonlinear Waves*, 1st ed., Wiley, New York, 1974.
- [37] Karpman, V.I., *Non-linear Waves in Dispersive Media*, 1st ed., Pergamon Press, New York, 1975.
- [38] Gardner, C.S. et al., Method for solving the Korteweg-deVries equation, *Phys. Rev. Lett.*, 19, 1095, 1967.
- [39] Landau, L.D. and Lifschitz, E.M., *Quantum Mechanics, Non-relativistic Theory*, 2nd ed., Pergamon Press, New York, 1965.
- [40] Fermi, E., Pasta, J. and Ulam, S., Tech. Rep. LA-1940, Los Alamos, NM, 1955.
- [41] Toda, M., *Theory of Nonlinear Lattices.*, 1st ed., Springer-Verlag, Berlin, 1981.
- [42] Potapov, A.I. et al., Nonlinear interactions of solitary waves in a 2D lattice, *Wave Motion*, 34, 83, 2001.
- [43] Meijer, H.G.E., Master's Thesis, University of Utrecht, 2003.
- [44] Kadomtsev, B.B. and Petviashvili, V.I., On the stability of solitary waves in weakly dispersive media, *Soviet Phys. Dokl.*, 15, 539, 1970.
- [45] Infeld, E., Senatorski, A., and Skorupski, A.A., Numerical simulations of KP soliton interactions, *Phys. Rev. E*, 51(4), 3183, 1995.
- [46] Driscoll, T.A., A composite Runge-Kutta method for the spectral solution of semilinear PDE, *J. Comp. Phys.*, 182, 357, 2002.
- [47] Balogh, A. and Krstic, M., Boundary control of the KdV-Burgers equation, *IEEE Trans. Autom. Contr.*, 45(9), 1739, 2000.
- [48] Damen, E.P.N. et al., Generation and propagation of coherent phonon beams, *Phys. Rev. B*, 64, 174303, 2001.

- [49] Singhsomroje, W. and Maris H.J., Generating and detecting phonon solitons in MgO using picosecond ultrasonics, *Phys. Rev. B*, 69, 174303, 2004.
- [50] Damen, E.P.N, Arts, A.F.M., and De Wijn, H.W., Experimental verification of Herring's theory of anharmonic phonon relaxation: TeO₂, *Phys. Rev. B*, 59(1), 349, 1999.
- [51] Muskens, O.L. and Dijkhuis, J.I., Propagation of ultrashort acoustic wave packets in PbMoO₄ studied by Brillouin spectroscopy, *Physica B*, 316-317, 373, 2002.
- [52] Muskens, O.L. and Dijkhuis, J.I., Trains of ultrashort acoustic solitons, *Phys. Stat. Sol.*, to be published, 2005.